Quantitative 3D imaging of whole, unstained cells by using X-ray diffraction microscopy

Huaidong Jiang[a,2], Changyong Song[b], Chien-Chun Chen[a], Rui Xu[a], Kevin S. Raines[a], Benjamin P. Fahimian[a], Chien-Hung Lu[c], Ting-Kuo Lee[c], Akio Nakashima[d], Jun Urano[d], Tetsuya Ishikawa[b], Fuyuhiko Tamanoi[d], and Jianwei Miao[a,1]

[a]Department of Physics and Astronomy and California NanoSystems Institute, University of California, Los Angeles, CA 90095; [b]RIKEN SPring-8 Center, 1-1-1, Kouto, Sayo, Hyogo 679-5148, Japan; [c]Institute of Physics, Academia Sinica, Nankang, Taipei 11529, Taiwan; and [d]Department of Microbiology, Immunology, and Molecular Genetics, University of California, Los Angeles, CA 90095

Edited* by Margaret M. Murnane, University of Colorado, Boulder, CO, and approved April 30, 2010 (received for review January 5, 2010)

Microscopy has greatly advanced our understanding of biology. Although significant progress has recently been made in optical microscopy to break the diffraction-limit barrier, reliance of such techniques on fluorescent labeling technologies prohibits quantitative 3D imaging of the entire contents of cells. Cryoelectron microscopy can image pleomorphic structures at a resolution of 3–5 nm, but is only applicable to thin or sectioned specimens. Here, we report quantitative 3D imaging of a whole, unstained cell at a resolution of 50–60 nm by X-ray diffraction microscopy. We identified the 3D morphology and structure of cellular organelles including cell wall, vacuole, endoplasmic reticulum, mitochondria, granules, nucleus, and nucleolus inside a yeast spore cell. Furthermore, we observed a 3D structure protruding from the reconstructed yeast spore, suggesting the spore germination process. Using cryogenic technologies, a 3D resolution of 5–10 nm should be achievable by X-ray diffraction microscopy. This work hence paves a way for quantitative 3D imaging of a wide range of biological specimens at nanometer-scale resolutions that are too thick for electron microscopy.

coherent diffractive imaging | equally sloped tomography | lensless imaging | iterative phase-retrieval algorithms | oversampling

Application of the long penetration depth of X-rays to the imaging of large, unstained biological specimens has long been recognized as a possible solution to the thickness restrictions of electron microscopy. Indeed, using sizable protein crystals, X-ray crystallography is currently the primary methodology used for determining the 3D structure of protein molecules at near-atomic or atomic resolution. However, many biological specimens such as whole cells, cellular organelles, some viruses, and many important protein molecules are difficult or impossible to crystallize and hence their structures are not accessible by crystallography. Overcoming these limitations requires the employment of different techniques. One promising approach currently under rapid development is coherent diffraction microscopy (also termed coherent diffractive imaging or lensless imaging) in which the coherent diffraction pattern of a noncrystalline specimen or a nanocrystal is measured and then directly phased to obtain an image (1–28). The well-known phase problem is solved by using the oversampling method (29) in combination with the iterative algorithms (30–33). Since its first experimental demonstration in 1999 (1), coherent diffraction microscopy has been applied to imaging a wide range of materials science and biological specimens such as nanoparticles, nanocrystals, biomaterials, cells, cellular organelles, viruses by using synchrotron radiation (2–21), high harmonic generation (22–24), soft X-ray laser sources (23, 25), and free electron lasers (26–28). Until now, however, the radiation damage problem and the difficulty of acquiring high-quality 3D diffraction patterns from individual whole cells have prevented the successful high-resolution 3D imaging of biological cells by X-ray diffraction microscopy. Here, we report 3D quantitative imaging of a whole, unstained yeast spore at a resolution of 50–60 nm. We identified the internal cellular structures including spore wall, nucleus, nucleolus, vacuole, endoplasmic reticulum, mitochondria, and granules in three dimensions.

In this study, we chose to image *Schizosaccharomyces pombe* yeast spores due to their significance as a model organism in cellular biology and their relative radiation robustness to X-rays. One important property of the yeast life cycle is that, when encountering low nutrient conditions, formation of spores is often initiated (34). Two different mating types of cells undergo sexual development leading to the formation of four spores within a cell. Major structural and morphological changes occur during the spore formation. The *S. pombe* yeast spore samples were freshly prepared (*Materials and Methods*). After fixation, unstained yeast spores were suspended in deionized water and supported on 30-nm-thick silicon-nitride membranes. Single, well-isolated spores were located with an optical microscope and studied by the X-ray diffraction microscope.

The experiment was carried out on an undulator beamline (BL29) at SPring-8. Fig. 1 shows the schematic layout of the 3D X-ray diffraction microscope. A coherent X-ray beam with energy of 5 keV was defined by a 20-μm pinhole, which was mounted at a distance of 1.49 m upstream of the sample. A silicon aperture with beveled edges was positioned just in front of the sample to serve as a guard slit and to eliminate the stray scattering from the pinhole. The sample was mounted on a rotation stage for 3D data acquisition. The diffraction intensity was measured by a liquid-nitrogen-cooled CCD camera with 1340×1300 pixels and a pixel size of 20×20 μm^2. A beamstop was positioned just in front of the CCD to block the direct beam. To enable direct phase retrieval, the diffraction intensity was sampled on the CCD with a spacing finer than the inverse of the sample size (i.e., oversampling) (29). The degree of oversampling was controlled by adjusting the distance between the sample and the CCD, which was set 1.26 m in this experiment. To enhance the dynamic range of the diffraction intensity, a low-resolution (LR) and a high-resolution (HR) diffraction patterns were measured from an unstained yeast spore at each tilt angle. The acquisition time for each LR pattern was about 0.5 s/exposure with 2,000 exposures, and for each HR pattern was about 50 s/exposure with 80 exposures. The LR and HR patterns were then used to assemble a complete 2D diffraction pattern. Fig. 2*A* shows a representative 2D diffraction pattern. To enable quantitative image reconstruction, we ensured the missing center (i.e., the center intensities blocked by the beamstop) confined within the

Author contributions: H.J., C.S., T.I., F.T., and J.M. designed research; H.J., C.S., C.-C.C., R.X., K.S.R., C.-H.L., A.N., J.U., F.T., and J.M. performed research; H.J., C.S., C.-C.C., R.X., K.S.R., B.P.F., T.-K.L., and J.M. analyzed data; and H.J. and J.M. wrote the paper.

The authors declare no conflict of interest.

*This Direct Submission article had a prearranged editor.

[1]To whom correspondence should be addressed. E-mail: miao@physics.ucla.edu.

[2]Present address: State Key Laboratory of Crystal Materials, Shandong University, Jinan 250100, China.

This article contains supporting information online at www.pnas.org/lookup/suppl/doi:10.1073/pnas.1000156107/-/DCSupplemental.

www.pnas.org/cgi/doi/10.1073/pnas.1000156107

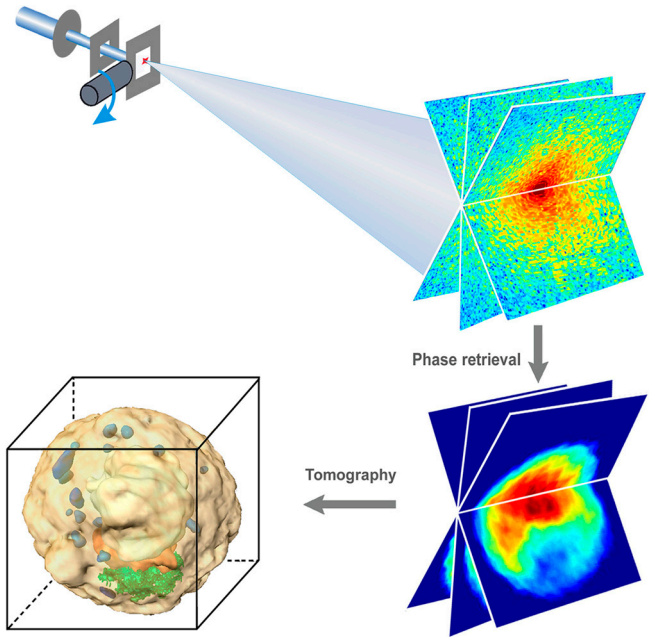

Fig. 1. Schematic layout of the 3D X-ray diffraction microscope. A 20 μm pinhole and a guard slit were used to define a clean X-ray beam. Oversampled diffraction patterns, measured on a CCD camera, were directly phased to obtain 2D projectional images. The 3D image of a whole cell was reconstructed from the set of 2D projectional images by a tomographic method.

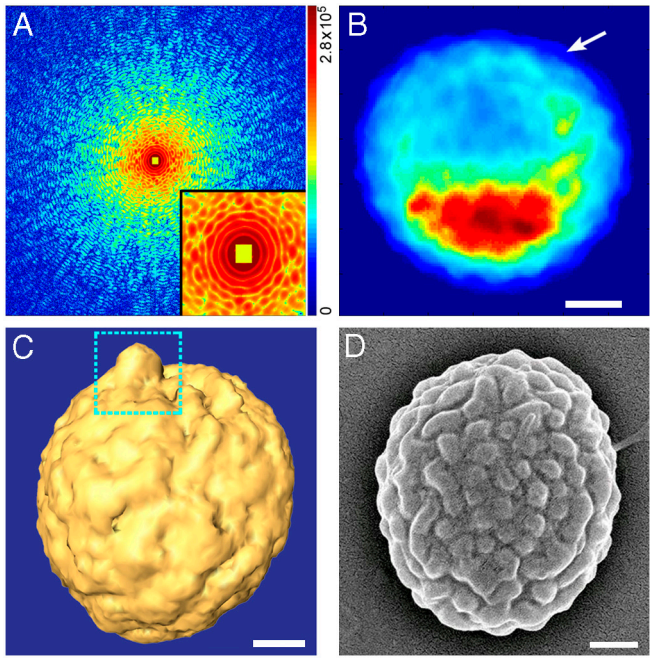

Fig. 2. Representative diffraction pattern and reconstructions of a whole yeast spore cell. (*A*) A 2D diffraction pattern (768 × 768 pixels) measured from the yeast spore. The diffraction intensity, displayed in a logrithmatic scale (zero valued pixels are set to a very small number to avoid infinity), extends to $q = 24.6\ \mu m^{-1}$ at the edge. The inset shows the missing center (15 × 17 pixels) is confined within the centro-speckle. Color scale shows the number of photons. (*B*) The corresponding reconstructed projectional image. The arrow indicates the thick spore wall, which was estimated to be ~120 nm. (*C*) Isosurface rendering of the reconstructed 3D image where the rough surface of the yeast spore is clearly visible. The dotted square indicates that a sporeline likely protrudes from the spore surface. (*D*) SEM image of a different yeast spore formed at the same condition. (Scale bar: 500 nm.)

centro-speckle (35), shown in Fig. 2*A*, *Inset*. To obtain a 3D dataset, we acquired a set of 25 complete 2D diffraction patterns by tilting the sample from −69.4° to +69.4°. The diffraction patterns between ±69.4° and ±90° were not measurable due to the interference of the sample holder with the incident beam at these tilt angles, which constitutes the missing wedge problem. The total radiation dose to the sample was estimated to be 5.25×10^8 Gy (*Materials and Methods*). To examine the effect of radiation dose on the cell structure, we took two diffraction patterns at the same tilt angle before and after acquisition of the full 3D dataset. A quantitative comparison of the two diffraction patterns indicated that the structural changes due to the radiation dose are negligible at this spatial resolution.

When the diffraction intensity is oversampled such that the number of independently measured intensity points is more than the number of unknown variables of the sample, the phases are in principle uniquely encoded in the diffraction intensity (29) and can be directly retrieved by using iterative algorithms (30–33). In this experiment, we first reconstructed projectional images from individual 2D diffraction patterns by an iterative algorithm (32), where a projectional image represents the integral of the sample along the x-ray beam direction at a certain orientation. We then computed the 3D structure of the yeast spore cell from the set of projectional images through tomographic reconstruction. Due to radiation damage to biological specimens, the X-ray flux per projection as well as the number of projections have to be limited, resulting in noisy diffraction patterns that make the phase retrieval and tomographic reconstruction somewhat problematic. To enhance the signal-to-noise ratio, we first numerically integrated the diffraction intensity by binning 3 × 3 pixels into 1 pixel, and then removed the error due to intensity integration through deconvolution (36). The size of each diffraction pattern was reduced from 768 × 768 pixels to 256 × 256 pixels.

The phase retrieval of each diffraction pattern was conducted by a variation of the GHIO (Guided Hybrid Input and Output) algorithm (32), which incorporates edge-preserving image regularization in order to guide the phase retrieval to the less noisy state that is concurrently consistent with experimental data. The GHIO algorithm began with 16 different random initial phase seeds and the quality of each reconstruction was monitored by an *R* factor (R_F),

$$R_F = \frac{\sum_{k_x,k_y} ||F^m(k_x,k_y)| - |F^c(k_x,k_y)||}{\sum_{k_x,k_y} |F^m(k_x,k_y)|}, \quad [1]$$

where $|F^m(k_x,k_y)|$ and $|F^c(k_x,k_y)|$ are the measured and calculated Fourier modulus, respectively. To optimize the initial random phase seeds, we generated each of the 16 seeds from 40 random phase sets by choosing the smallest *R* factor after a number of iterations (25). Additionally, for a portion of the iterations we supplemented the GHIO algorithm with image regularization through the total-variation minimization on the image which allows for edge preserving and suppression of noise. The total-variation minimization was computed by the Rudin–Osher–Fatemi technique (37). In order to ensure complete consistency with experimental data, the regularization was lifted in the last cycle of iterations. In each GHIO reconstruction, we first employed a rectangular loose support and then updated it with a rectangular tight support. The size of the tight support depends on the tilt angles, which ranges from 131 × 123 pixels to 131 × 89 pixels. The GHIO algorithm was terminated after the *R* factors became stabilized, which were around 6–8%.

Fig. S1 shows the 25 final images reconstructed from the diffraction patterns with tilt angles ranging from −69.4° to +69.4°. The final image of each GHIO run was obtained by averaging the five best images with the smallest *R* factors. To illustrate the

accuracy of the reconstructions, we performed a few independent GHIO runs on each 2D diffraction pattern. Fig. S2*A* shows two representative final images reconstructed from the same diffraction pattern. The line scans (Fig. S2*B*) and the quantitative comparison indicate the consistency of the independently reconstructed images (*SI Text*).

The 25 projectional images, reconstructed from the 2D diffraction patterns, were used for the 3D tomographic reconstruction. This process consists of two steps: aligning the projectional images to a common tilt axis and then performing 3D tomographic reconstruction. Because the projectional images can have an arbitrary shift along the x and y axes, they must be aligned before the 3D reconstruction. Although there exists a variety of image alignment approaches, we chose the method based on the moment of charge density distribution (38), which has been experimentally tested (12). Using this method, we aligned the 25 images to a common tilt axis (*Materials and Methods*). The 3D image reconstruction was computed by the equally sloped tomography (EST) method (39, 40). Because only a limited number of projections was acquired due to concerns about radiation damage to the yeast spore cell, conventional tomographic reconstruction methods, such as filtered back projection (FBP), do not usually yield satisfactory results. To address this problem, the EST method, an iterative reconstruction method that aims to solve for a portion of the missing projection data, was employed for the tomographic reconstruction. The EST method is coupled with an acquisition scheme for which the projections are acquired at equal slope intervals, instead of equal angle intervals, which results in the elimination of interpolative inaccuracies in conventional tomographic methods (12, 39, 40). EST iterates back and forth between real and reciprocal space. In real space, the negative density and the density outside a support are pushed to zeros. Unlike the phase-retrieval algorithms which usually require a tight support, EST performs well with a loose support. In reciprocal space, the Fourier coefficients with both the magnitudes and phases, which are obtained from the reconstructed projections, are updated in each iteration, while the other Fourier coefficients remain unchanged. The convergence of EST is monitored by an error function, defined as the difference between the calculated Fourier coefficients and those obtained from the experimental data (39, 40). In our reconstructions, we terminated the algorithm after ~150 iterations when the error function became stabilized. Both numerical simulations and experimental results from cryoelectron microscopy have indicated that EST produces superior results relative to FBP and the algebraic reconstruction technique when there is a limited number of projections as well as the missing wedge problem (12, 39, 40). After the 3D image was obtained by EST, we verified the fidelity of the reconstruction by calculating 25 diffraction patterns from the reconstructed 3D image. We then compared these computed diffraction patterns to the measured ones and found good agreement, thus confirming the fidelity of the 3D reconstruction.

To estimate the resolution achieved, we first calculated the spatial resolution of the diffraction patterns by $d = \lambda/2\sin(\theta)$ where λ is the wavelength and 2θ is the diffraction angle subtended by the distance from the center to the edge of the CCD. In this experiment, $\lambda = 2.48$ Å, and the distance from the center to the edge of the CCD is 7.68 mm. Thus we obtained $\theta = 0.174°$ and $d = 41$ nm (i.e., a pixel size of 20.5 nm). Fig. S3 shows the power spectrum density of a representative 2D diffraction pattern, indicating the diffraction signal actually extends beyond a spatial resolution of 40 nm. Based on the estimated pixel size, we quantified the 3D resolution of the reconstructed image by using the phase-retrieval transfer function (PRTF) (8, 10) (*SI Text*). Fig. S4 *A* and *B* show the PRTF curves for the tilt angles of 0° and 69.4°, respectively. Based on the criterion of PRTF = 0.5, we estimated the 3D resolution to be 50–60 nm (*SI Text*). We further verified the 3D resolution by plotting the density variation across an exemplary

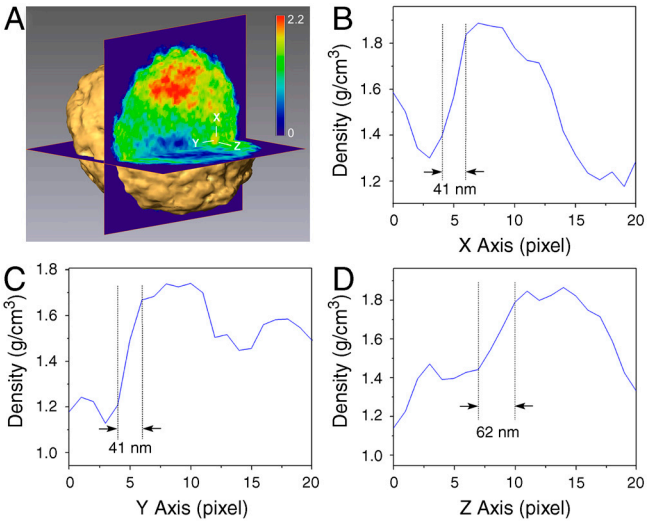

Fig. 3. Quantification of the 3D resolution. (*A*) The density variation across a mitochondrion was plotted along the *x*, *y*, and *z* axes, which was used to estimate the 3D resolution of the reconstructed yeast spore. Color scale is in g/cm^3. (*B* and *C*) A resolution of ~41 nm (i.e., 2 pixels) along the *x* and *y* axes was achieved. (*D*) A resolution of ~62 nm (i.e., 3 pixels) along the *z* axis was achieved.

mitochondrion (Fig. 3), indicating a resolution of ~41 nm (i.e., the full width at half maximum) along the x and y axes and ~62 nm along the z axis. Both the PRTF and the line plotting across a mitochondrion confirmed a 3D resolution of 50–60 nm achieved in this experiment.

Results and Discussion

Fig. 2 *A* and *B* show a representative 2D diffraction pattern and the corresponding projectional image of the unstained yeast spore. The colors in the projectional image represent variation in density. One distinctive feature in Fig. 2*B* is the thick yeast spore wall. We estimated the thickness of the spore wall to be ~120 nm, which is consistent with measurements from sectioned transmission electron microscope images (41). The cellular organelles are not readily distinguishable in the 2D projectional image due to the overlapping of the complex structures inside the cell. Fig. 2*C* shows an isosurface rendering of the reconstructed 3D image. The rough surface of the yeast spore is clearly visible, which is consistent with the SEM image (Fig. 2*D*, a different yeast spore formed under the same conditions) as well as the previous report (42).

By measuring the incident and diffracted X-ray intensities, we quantified the density of the reconstructed 3D image (43) (*Materials and Methods*). The average density of the yeast spore was determined to be ~1.14 g/cm^3, which is in good agreement with other measurements (44). Based on the intrinsic density variation, we identified the cellular organelles in the yeast spore cell (*Materials and Methods*). Fig. 4*A* shows a volume rendering of the 3D image, in which the nucleus is in orange, the endoplasm reticulum (ER) in green, the vacuole in white, the mitochondria in blue and the granules are in light blue (Movie S1). The outermost layer of the spore was omitted in order to illustrate the internal structures. Fig. 4*B* shows a zoomed view of the mitochondria, the ER, and the nucleus. The mitochondria with an elongated shape have relatively high density and their length was estimated to be ~200–300 nm. The network-like structure of the ER, composed of fibril-like structure connecting the nucleus and the spore membrane, was visualized. The nucleus exhibits a very high density with a volume of 0.28 μm^3, which accounts for ~5% of the cell volume. A region near the center of the nucleus has the highest density in the cell, which is likely the nucleolus (Fig. 4*B*, *Inset*). The highest density is possibly related to the condensation of

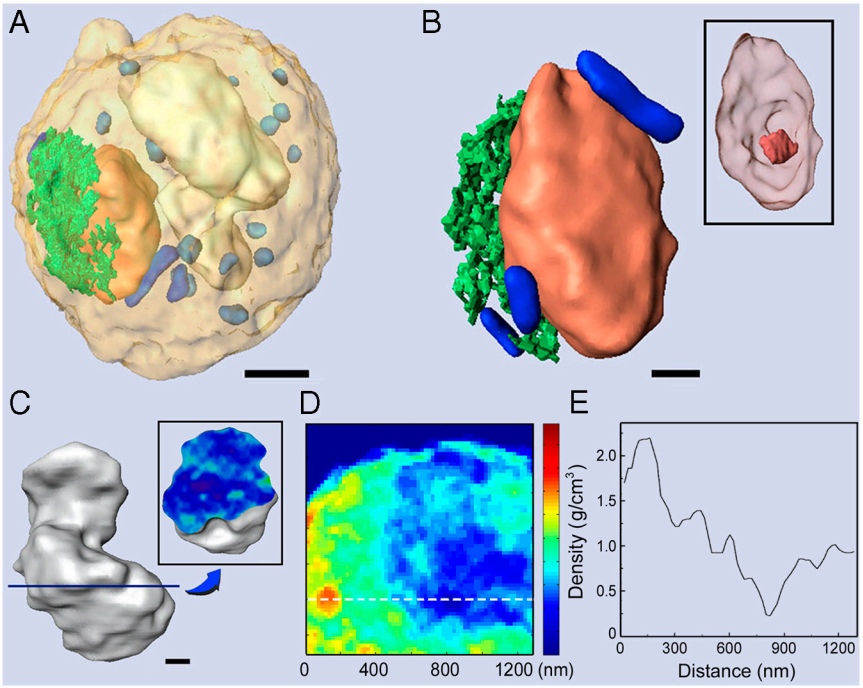

Fig. 4. Three-dimensional visualization of the cellular organelles inside the yeast spore cell. (*A*) A 3D volume rendering of the reconstructed yeast spore, showing nucleus (orange), ER (green), vacuole (white), mitochondria (blue), and granules (light blue). (Scale bar: 500 nm.) (*B*) Zoomed view of the 3D morphology and structure of the nucleus, ER, and mitochondria. Inset shows the nucleolus (orange). (Scale bar: 200 nm.) (*C*) A 3D morphology and structure of the vacuole. Inset shows a cross-sectional image of the vacuole. (Scale bar: 200 nm.) (*D* and *E*) A thin slice of the reconstructed yeast spore and a line scan along the dashed line, showing the density variation across a mitochondrion and the vacuole.

the chromatin. The nuclear size is regulated by several cellular functions such as nucleocytoplasmic transport, lipid metabolism, and ribosome biogenesis. Our imaging technique provides a quantitative approach to directly measure the size, morphology, structure, and density of these organelles. Fig. 4*C* shows the 3D structure of the vacuole, having an irregular 3D morphology. The volume of the vacuole was determined to be ~0.7 μm^3, which accounts for ~12% of the spore volume. The cross-sectional image (Fig. 4*C*, *Inset*) indicates the existing of high-density spots inside the vacuole, which may be vacuolar granules and aggregation of proteins. A thin slice of the reconstructed yeast spore and a line scan across the slice are illustrated in Fig. 4 *D* and *E*, showing the density variation across a mitochondrion and the vacuole.

Yeast spores germinate when they encounter enriched nutrient conditions. The germination process includes four successive steps: a loss of refractility (darkening) of spores, protrusion of a new cell body, nuclear division, and septation. A genetic program dictates this germination process, in which the cAMP-PKA (protein kinase A) pathway and Ras signaling pathway are known to play an important role (45). In our reconstructed yeast spore structure, we observed a 3D structure protruding from the spore surface, shown in Fig. 2*C* (the squared region). To visualize the 3D internal structure of the protruded region, we numerically sectioned it slice by slice along two perpendicular directions. Fig. 5 *A* and *B* shows a series of successive slices of the 3D structure along the horizontal and vertical directions, respectively, with each slice being 20.5-nm thick. A high-density region (white arrow) and a low-density region (yellow arrow) are clearly visible.

Conclusion

We have demonstrated quantitative 3D imaging of a whole, unstained yeast spore cell at a resolution of 50–60 nm by X-ray diffraction microscopy, and quantified the 3D morphology and structure of the internal cellular organelles in the cell. Compared to lens-based soft X-ray microscopy (46), the resolution of X-ray diffraction microscopy is ultimately limited by radiation damage

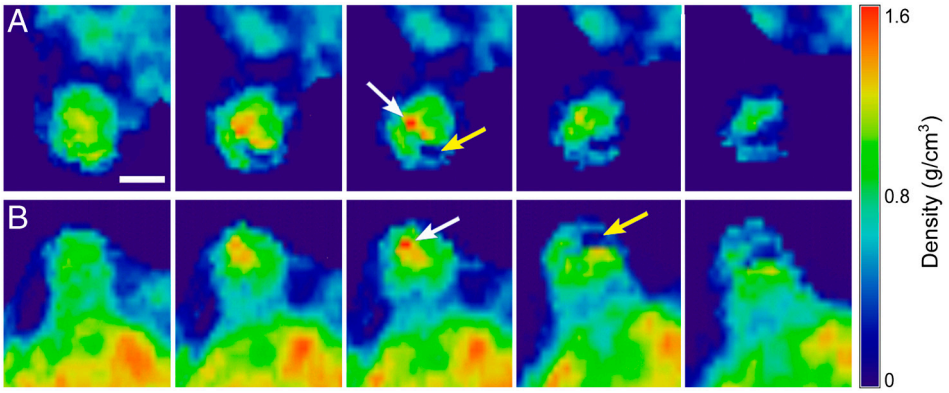

Fig. 5. Successive slices of the sporeline along the horizontal (*A*) and vertical (*B*) directions with each slice being 20.5-nm thick. A high-density region (white arrow) and a low-density region (yellow arrow) are clearly visible. (Scale bar: 200 nm.)

to biological specimens. Using cryogenic technologies, the radiation damage problem can be mitigated (19, 20), and a 3D resolution of 5–10 nm should be achievable (47, 48). Compared to superresolution optical microscopy (49), which allows for the selection of the fluorescently labeled molecules or molecular assemblies, X-ray diffraction microscopy is based on the intrinsic density variations of biological specimens, and accordingly, enables quantitative 3D imaging of the entire contents of cells and cellular organelles. Furthermore, due to the long penetration length of X-rays, this work may also be applied to imaging larger biological specimens such as tissue slices. As coherent X-ray sources, such as next-generation synchrotron radiation, X-ray-free electron lasers, high harmonic generation, and soft X-ray lasers, are currently under rapid development, this work enables the initiation of quantitative 3D imaging of a broad range of biological specimens at the nanometer-scale resolution using such emerging sources.

Materials and Methods

Sample Preparation. The cell used for the study was the fission yeast *Schizosaccharomyces pombe* spore, a homothallic haploid strain, which was freshly prepared as previously described (50). *S. pombe* strain FY155, provided by The Susan Forsburg Lab (www-rcf.usc.edu/~forsburg), was grown on the plate of yeast extract with supplements at 30 °C. The cells were picked from fresh colonies, streaked onto malt extract agar plate, and incubated for 3 days at 25 °C to induce mating, meiosis, and spore formation. After incubation, the cells, including nonmating haploid cells, zygotes, ascospores, and single spores, were treated with glusulase for 1 day to digest the cells except for spores. To fix spores with formaldehyde and glutaraldehyde, the obtained single spores were washed twice with sterile water and treated with 3.2% formaldehyde (final concentration) for 1 min, followed by adding 12% of glutaraldehyde to 0.25% of final concentration.

Radiation Dose Estimation for the Yeast Spore Cell. Quantifying the radiation dose to biological cells is an important issue as the cellular structure can, in principle, be altered at appreciable resolutions by the X-ray beam (47, 48). However, in this experiment we found that the structure changes due to the radiation dose are negligible at the achieved resolution. We verified this both experimentally and by calculating the total radiation dose delivered to the cell. Here, we detail the radiation dose calculation.

- The incident X-ray flux: Although the average beam intensity at SPring-8 BLXU-29 has been well characterized, we also used a silicon detector to measure the incident X-ray flux. This approach is more reliable as the beam was spatially filtered and the beam intensity might fluctuate during our experiment. We computed the incident X-ray flux from the silicon detector counts after a 20 μm pinhole,

$$F = n_e g w / E, \qquad [2]$$

where F is the X-ray flux, n_e the number of electron counts, g the amplifier gain, w the energy required to create an electron-hole pair in the silicon detector, and E the incident X-ray energy. In this experiment, w is 3.6 eV, g is 10^7, and E is 5 keV. For each measured angle, we acquired a LR and a HR diffraction patterns to enhance the dynamic range of the intensity. Generally, the silicon detector readout is $\sim 1.2 \times 10^5$ counts for the LR pattern and $\sim 1.6 \times 10^5$ counts for the HR pattern, where the monochromator was slightly adjusted to reduce the flux for measuring the LR pattern. The incident X-ray flux for the LR and HR patterns was estimated to be

$$\text{LR: } F_L = 0.86 \times 10^9 \text{ photons/s}$$
$$\text{HR: } F_H = 1.15 \times 10^9 \text{ photons/s} \qquad [3]$$

- The total incident X-ray photons per projection: The total acquisition time was about 1,000 s for each LR pattern and about 4,000 s for each HR pattern. The total incident X-ray photons (P_T) per projection was estimated to be

$$\text{LR: } F_L \Delta t_L = 0.86 \times 10^{12} \text{ photons}$$
$$\text{HR: } F_H \Delta t_H = 4.6 \times 10^{12} \text{ photons}$$
$$\text{Total: } P_T = F_L \Delta t_L + F_H \Delta t_H = 5.46 \times 10^{12} \text{ photons} \qquad [4]$$

- The total incident X-ray photons per projection and per unit area (through the 20 μm pinhole) was determined by

$$\eta P_T / A = 1.46 \times 10^{10} \text{ photons}/\mu\text{m}^2, \qquad [5]$$

where $\eta = 83.8\%$ is the fraction coefficient, taking into account the flux in the first speckle, and A the area of the pinhole.

- The radiation dose delivered to the yeast cell per projection was obtained as

$$\text{Dose} = (\eta P_T / A)\mu E / \rho = 2.1 \times 10^7 \text{ Gy}, \qquad [6]$$

where ρ is the density of the cell, μ is the linear absorption coefficient, and the mass absorption coefficient (μ/ρ) is 18 cm^2/g. Thus the total dose delivered to the yeast spore cell for the acquisition of the 3D dataset (i.e., 25 diffraction patterns) was about 5.25×10^8 Gy.

Alignment of the 25 Projectional Images. The reconstructed projectional images can have arbitrary shifts relative to each other along the x and y axes where the x axis is assumed to be the tilt axis and the incident X-ray beam is along the z axis. In our analysis, we first aligned the 25 images along the x axis by projecting each 2D image onto the x axis and then aligning the 25 projected 1D curves. To align the 25 images along the y axis, we first chose a reference coordinate with the origin at the center of the y axis, in which all the projections were assumed to be aligned. We then calculated the moment of charge density for each 2D image (38), which is similar to the calculation of the center of mass. By choosing the images with the tilt angles of $45° + \theta$ and $45° - \theta$ (i.e., symmetric along the 45° tilt angle), we calculated the y axis shift of each image relative to the reference coordinate based on the moment of charge density. The detailed alignment procedure can be found in ref. 40.

Quantification of Electron Density and Conversion from Electron to Mass Density. We quantified the electron density of the yeast spore by (43)

$$I(0,0) = I_0 r_e^2 |F(0,0)|^2 \frac{\Delta s}{r^2}, \qquad [7]$$

where $I(0,0)$ is the number of diffracted X-ray photons in the centro-pixel of the CCD, I_0 the incident X-ray flux per unit area, r_e the classical electron radius, $|F(0,0)|$ the Fourier modulus at the center pixel which is equal to the total number of electrons in the yeast spore, Δs the area of the centro-pixel, and r the distance from the sample to the CCD. Although I_0 was experimentally determined by a photodiode, $I(0,0)$ could not be directly measured due to the beamstop. To determine $I(0,0)$, we ensured the missing center confined within the centro-speckle (35), which enables recovering $I(0,0)$ directly from the measured diffraction intensities.

To convert the electron-to-mass density, we used the composition elemental formula of yeast, $C_1H_{1.56}O_{0.52}N_{0.16}$ (51), from which we estimated the percentage of the electrons in H, C, O, and N atoms. For C, O, and N, the atomic mass is approximately twice of the number of electrons. Thus the relationship between molecular weight (M) and the total number of electrons (N_e) is $M = 1.88N_e$. By using the volume of the reconstructed 3D structure, we converted electron-to-mass density for the yeast spore cell.

Identification of Internal Cellular Organelles. To identify the internal cellular organelles, we manually segmented the reconstructed 3D image and visualized each segment with Amira (Mercury Computer Systems). The initial assignment of the organelles in the segmented images was carried out on the basis of the density and the organelle appearance of the segmented objects. We determined the average density of each organelle and divided them into five categories, corresponding to different color scales. Based on the measured density, size, distribution, and morphology of each organelle, we identified the organelles, including nucleus, nucleolus, endoplasmic reticulum, vacuole, mitochondria, and granules inside the yeast spore. Fig. S5*A* shows 3D volume rendering of the yeast spore with cellular organelles identified, which is in good agreement with the corresponding 2D projection image at the same orientation, Fig. S5*B*.

ACKNOWLEDGMENTS. We thank Y. Nishino and Y. Kohmura for help with data acquisition, S. L. Forsburg for providing *Schizosaccharomyces pombe* strain FY155, and J. A. Rodríguez for stimulating discussions. This work was partially supported by the National Institutes of Health Grant GM081409-01A1 (to J.M.) and Grant CA41996 (to F.T.), the University of California Discovery Grant IT107-10166, and the US Department of Energy, Office of Basic Energy Sciences (DE-FG02-06ER46276). Use of the RIKEN beamline (BL29XUL) at SPring-8 was supported by RIKEN.

1. Miao J, Charalambous P, Kirz J, Sayre D (1999) Extending the methodology of X-ray crystallography to allow imaging of micrometre-sized non-crystalline specimens. *Nature* 400:342–344.
2. Robinson IK, Vartanyants IA, Williams GJ, Pfeifer MA, Pitney JA (2001) Reconstruction of the shapes of gold nanocrystals using coherent X-ray diffraction. *Phys Rev Lett* 87:195505.
3. Miao J, et al. (2002) High resolution 3D X-ray diffraction microscopy. *Phys Rev Lett* 89:088303.
4. Williams GJ, Pfeifer MA, Vartanyants IA, Robinson IK (2003) Three-dimensional imaging of microstructure in Au nanocrystals. *Phys Rev Lett* 90:175501.
5. Miao J, et al. (2003) Imaging whole Escherichia coli bacteria by using single particle X-ray diffraction. *Proc Natl Acad Sci USA* 100:110–112.
6. Marchesini S, et al. (2003) X-ray image reconstruction from a diffraction pattern alone. *Phys Rev B* 68:140101.
7. Nugent KA, Peele AG, Chapman HN, Mancuso AP (2003) Unique phase recovery for nonperiodic objects. *Phys Rev Lett* 91:203902.
8. Shapiro D, et al. (2005) Biological imaging by soft X-ray diffraction microscopy. *Proc Natl Acad Sci USA* 102:15343–15346.
9. Pfeifer MA, Williams GJ, Vartanyants IA, Harder R, Robinson IK (2006) Three-dimensional mapping of a deformation field inside a nanocrystal. *Nature* 442:63–66.
10. Chapman HN, et al. (2006) High-resolution ab initio three-dimensional X-ray diffraction microscopy. *J Opt Soc Am A* 23:1179–1200.
11. Williams GJ, et al. (2006) Fresnel coherent diffractive imaging. *Phys Rev Lett* 97:025506.
12. Miao J, et al. (2006) Three-dimensional GaN-Ga_2O_3 core shell structure revealed by X-ray diffraction microscopy. *Phys Rev Lett* 97:215503.
13. Abbey B, et al. (2008) Keyhole coherent diffractive imaging. *Nat Phy* 4:394–398.
14. Jiang H, et al. (2008) Nanoscale imaging of mineral crystals inside biological composite materials using X-ray diffraction microscopy. *Phys Rev Lett* 100:038103.
15. Rodenburg J, et al. (2007) Hard-x-ray lensless imaging of extended objects. *Phys Rev Lett* 98:034801.
16. Thibault P, et al. (2008) High-resolution scanning X-ray diffraction microscopy. *Science* 321:379–382.
17. Song C, et al. (2008) Quantitative imaging of single, unstained viruses with coherent X-rays. *Phys Rev Lett* 101:158101.
18. Nishino Y, Takahashi Y, Imamoto N, Ishikawa T, Maeshima K (2009) Three-dimensional visualization of a human chromosome using coherent X-ray diffraction. *Phys Rev Lett* 102:018101.
19. Huang X, et al. (2009) Soft X-ray diffraction microscopy of a frozen hydrated yeast cell. *Phys Rev Lett* 103:198101.
20. Lima E, et al. (2009) Cryogenic X-ray diffraction microscopy for biological samples. *Phys Rev Lett* 103:198102.
21. Giewekemeyer K, et al. (2010) Quantitative biological imaging by ptychographic x-ray diffraction microscopy. *Proc Natl Acad Sci USA* 107:529–534.
22. Sandberg RL, et al. (2007) Lensless diffractive imaging using tabletop, coherent, high harmonic soft X-ray beams. *Phys Rev Lett* 99:098103.
23. Sandberg RL, et al. (2008) High numerical aperture tabletop soft x-ray diffraction microscopy with 70 nm resolution. *Proc Natl Acad Sci USA* 105:24–27.
24. Ravasio A, et al. (2009) Single-shot diffractive imaging with a table-top femtosecond soft X-ray laser-harmonics source. *Phys Rev Lett* 103:028104.
25. Raines KS, et al. (2010) Three-dimensional structure determination from a single view. *Nature* 463:214–217.
26. Chapman HN, et al. (2006) Femtosecond diffractive imaging with a soft-x-ray free-electron laser. *Nat Phy* 2:839–843.
27. Barty A, et al. (2008) Ultrafast single-shot diffraction imaging of nanoscale dynamics. *Nat Photonics* 2:415–419.
28. Mancuso AP, et al. (2009) Coherent-pulse 2D crystallography using a free-electron laser X-ray source. *Phys Rev Lett* 102:035502.
29. Miao J, Sayre D, Chapman HN (1998) Phase retrieval from the magnitude of the Fourier transforms of non-periodic objects. *J Opt Soc Am A* 15:1662–1669.
30. Fienup JR (1982) Phase retrieval algorithms: A comparison. *Appl Opt* 21:2758–2769.
31. Elser V (2003) Solution of the crystallographic phase problem by iterated projection. *Acta Crystallogr A* 59:201–209.
32. Chen CC, Miao J, Wang CW, Lee TK (2007) Application of the optimization technique to non-crystalline X-ray diffraction microscopy—guided hybrid input-output method (GHIO). *Phys Rev B* 76:064113.
33. Marchesini S (2007) Phase retrieval and saddle-point optimization. *J Opt Soc Am A* 24:3289–3296.
34. Leupold U (1970) Genetical methods for Schizosaccharomyces pombe. *Method Cell Physiol*, ed DM Prescott (Academic, New York), Vol 4, pp 169–177.
35. Miao J, et al. (2005) Quantitative image reconstruction of GaN quantum dots from oversampled diffraction intensities alone. *Phys Rev Lett* 95:085503.
36. Song C, et al. (2007) Phase retrieval from exactly oversampled diffraction intensity through deconvolution. *Phys Rev B* 75:012102.
37. Rudin LI, Osher S, Fatemi E (1992) Nonlinear total variation based noise removal algorithms. *Physica D* 60:259–268.
38. Chen CC, Miao J, Lee TK (2009) Tomographic image alignment in 3D coherent diffraction microscopy. *Phys Rev B* 79:052102.
39. Miao J, Förster F, Levi O (2005) Equally sloped tomography with oversampling reconstruction. *Phys Rev B* 72:052103.
40. Lee E, et al. (2008) Radiation dose reduction and image enhancement in biological imaging through equally sloped tomography. *J Struct Biol* 164:221–227.
41. Tougan T, Chiba Y, Kakihara Y, Hirata A, Nojima H (2002) Meu10 is required for spore wall maturation in Schizosaccharomyces pombe. *Genes Cells* 7:217–231.
42. Nakamura T, Abe H, Hirata A, Shimoda C (2004) ADAM family protein Mde10 is essential for development of spore envelopes in the fission yeast *Schizosaccharomyces pombe*. *Eukaryot Cell* 3:27–39.
43. Miao J, Amonette J, Nishino Y, Ishikawa T, Hodgson KO (2003) Direct determination of the absolute electron density of nanostructured and disordered materials at sub-10 nm resolution. *Phys Rev B* 68:012201.
44. Kubitschek HE, Ward RA (1985) Buoyant density constancy of Schizosaccharomyces pombe cells. *J Bacteriol* 162:902–904.
45. Hatanaka M, Shimoda C (2001) The cyclic AMP/PKA signal pathway is required for initiation of spore germination in *Schizosaccharomyces pombe*. *Yeast* 18:207–217.
46. Parkinson DY, McDermott G, Etkin LD, Le Gros MA, Larabell CA (2008) Quantitative 3-D imaging of eukaryotic cells using soft X-ray tomography. *J Struct Biol* 162:380–386.
47. Shen Q, Bazarov I, Thibault P (2004) Diffractive imaging of nonperiodic materials with future coherent X-ray sources. *J Synchrotron Radiat* 11:432–438.
48. Howells MR, et al. (2009) An assessment of the resolution limitation due to radiation-damage in X-ray diffraction microscopy. *J Electron Spectrosc Rel Phenom* 170:4–12.
49. Chi KR, et al. (2009) Super-resolution microscopy. *Nat Method* 6:15–32 Special issue.
50. Moreno S, Klar A, Nurse P (1991) Molecular genetic analysis of fission yeast *Schizosaccharomyces pombe*. *Methods Enzymol* 194:795–823.
51. Kemp RB, Gallagher P, eds. (1999) *Thermal Analysis and Calorimetry, From Macromolecules to Man* (Elsevier, Amsterdam), Vol 4 p 296.